

**Signal-based AI-driven software solution for automated quantification of
metastatic bone disease and treatment response assessment using
Whole-Body Diffusion-Weighted MRI (WB-DWI) biomarkers
in Advanced Prostate Cancer**

*Antonio Candito¹, Matthew D Blackledge¹, Richard Holbrey¹, Nuria Porta¹, Ana Ribeiro²,
Fabio Zugni³, Luca D'Erme⁴, Francesca Castagnoli^{1,2}, Alina Dragan^{1,2}, Ricardo Donners⁵,
Christina Messiou^{1,2}, Nina Tunariu^{1,2}, and Dow-Mu Koh^{1,2}*

¹The Institute of Cancer Research, London, United Kingdom

²The Royal Marsden NHS Foundation Trust, London, United Kingdom

³ Department of Radiology, IEO European Institute of Oncology IRCCS, Milan, Italy

⁴Universita' del Sacro Cuore, Rome, Italy

⁵University Hospital Basel, Basel, Switzerland

Corresponding Author: Prof. Dow-Mu Koh
The Royal Marsden NHS Foundation Trust (UK)
dow-mu.koh@icr.ac.uk

Keywords: AI-driven Imaging Analysis; Whole-Body Diffusion-Weighted MRI (WB-DWI);
Quantitative Imaging Biomarkers; Metastatic Bone Disease; Treatment Response Assessment

ABSTRACT

Objective: Quantitative assessment of treatment response in Advanced Prostate Cancer (APC) with bone metastases remains an unmet clinical need. Whole-Body Diffusion-Weighted MRI (WB-DWI) provides two response biomarkers: Total Diffusion Volume (TDV) and global Apparent Diffusion Coefficient (gADC). However, tracking post-treatment changes of TDV and gADC from manually delineated lesions is cumbersome and increases inter-reader variability. We developed a software to automate this process.

Approach: Core technologies include: (i) a weakly-supervised Residual U-Net model generating a skeleton probability map to isolate bone; (ii) a statistical framework for WB-DWI intensity

normalisation, obtaining a signal-normalised $b=900\text{s/mm}^2$ (b900) image; and (iii) a shallow convolutional neural network that processes outputs from (i) and (ii) to generate a mask of suspected bone lesions, characterised by higher b900 signal intensity due to restricted water diffusion. This mask is applied to the gADC map to extract TDV and gADC statistics. We tested the tool using expert-defined metastatic bone disease delineations on 66 datasets, assessed repeatability of imaging biomarkers (N=10), and compared software-based response assessment with a *construct reference standard* based on clinical, laboratory and imaging assessments (N=118).

Main results: Dice score between manual and automated delineations was 0.6 for lesions within pelvis and spine, with an average surface distance of 2mm. Relative differences for log-transformed TDV (log-TDV) and median gADC were below 9% and 5%, respectively. Repeatability analysis showed coefficients of variation of 4.57% for log-TDV and 3.54% for median gADC, with intraclass correlation coefficients above 0.9. The software achieved 80.5% accuracy, 84.3% sensitivity, and 85.7% specificity in assessing response to treatment compared to the *construct reference standard*. Computation time generating a mask averaged 90 seconds per scan.

Significance: Our software enables reproducible TDV and gADC quantification from WB-DWI scans for monitoring metastatic bone disease response, thus providing potentially useful measurements for clinical decision-making in APC patients.

1. Introduction

Bone is the most common site for cancer spread in patients with Advanced Prostate Cancer (APC), with 90% of these patients developing metastatic bone disease. In up to 45% of these cases, the skeleton is the sole site of metastases [1], [2]. Metastatic bone disease significantly increases morbidity, leading to severe complications such as bone fractures and spinal cord compression, and is associated with a low five-year survival rate [3]. Although innovative targeted therapies have shown promise in clinical trials by improving quality of life, preventing complications, and extending survival for APC patients [4]–[6], treatments ultimately stop being effective. Therefore, it is imperative for clinicians to use advanced diagnostic tools to determine when to switch to a different drug to maintain the therapeutic effect, with the aim of keeping the patients “better for longer”.

Conventional medical imaging techniques, such as radionuclide bone scan (BS) and computed tomography (CT), are widely used to assess metastatic bone disease [7], [8]. However, these techniques have low sensitivity in detecting malignant bone lesions, lack response criteria and are not reliable in identifying early signs of disease progression [9]–[11]. Prostate specific membrane antigen positron emission tomography (PSMA-PET) offers higher sensitivity for detecting metastatic bone lesions and evaluating disease extent in APC patients [12], [13]. However, PSMA-PET is costly and prone to false positives due to the treatment-related flare phenomenon [14].

Whole-body Diffusion-Weighted MRI (WB-DWI) is a non-invasive, radiation-free technique that provides excellent contrast between normal bone and malignant bone disease, enabling “at a glance” visual assessment of cancer spread throughout the skeleton with higher sensitivity than BS and CT, including detecting early disease progression [15]. On DWI, malignant bone disease appears high signal intensity on high b-values (typically $b=900 \text{ s/mm}^2$, $b900$) images, due to restricted water diffusion within cancerous tissue, associated with increased cell density [16]. In addition, DWI allows for the quantification of two response biomarkers: the Total Diffusion Volume (TDV, in millilitres), reflecting tumour burden, and the global Apparent Diffusion Coefficient (gADC), calculated from two or three b-

value images, which inversely correlates with tumour cellularity [17], [18]. Quantitative TDV and gADC have been shown to corroborate with response by laboratory test and clinical findings, providing objective measurements of treatment response in APC patients [19], [20]. However, a factor limiting the use of quantitative WB-DWI measurements is the lack of advanced software that enables automated analysis and rapid calculation of metastatic disease throughout the body. Manual delineation for TDV and gADC measurements is tedious, often taking an hour or more depending on the disease volume, making it impractical for clinical application [21].

Semi-automated tools have been developed to facilitate the delineation and summation of metastatic bone disease [22]–[25]. However, multiple manual steps are still required, including selecting WB-DWI sequences as input from the imaging study, adjusting contrast on b900 images to differentiate/delineate suspected bone lesions from background bone marrow, and refining the generated mask to remove non-skeletal structures with similar signal intensity than bone lesions (e.g., adjacent internal organs, spinal canal contents, nerve roots, lymph nodes). These manual steps can incur delays, disrupt radiologists' reporting workflow, and increase the inter-reader variability of measuring the TDV and gADC.

In this study, we developed and test a signal-based AI-driven software solution to automatically identify, segment and quantify metastatic bone disease in patients with APC. We hypothesise that automated delineation of bone regions with restricted diffusion could be used to estimate TDV and the associated gADC from pre- and post-treatment WB-DWI scans, thus be used to assess disease response of metastatic bone disease. To test this hypothesis, we evaluated the accuracy of our software using retrospective and prospective WB-DWI scans in APC patients for assessing treatment response. Furthermore, we derived and tested a *Response Evaluation Criteria* (REC) based on our automated TDV and gADC measurements and their percentage changes post-treatment. Our quantitative measurements could assist clinicians by providing a more objective paradigm for classifying patients as responders, stable, or with disease progression, thereby improving clinical decision-making.

2. Methods

2.1 Patient population

This study was approved by research and ethics committee, which waived the requirement for patient consent for both retrospective and prospective datasets. All data were fully anonymised, and the study was conducted in accordance with the Declaration of Helsinki (2013). The inclusion criteria included patients with confirmed APC with bone metastases who were about to start systemic treatment or change to a new line of therapy, with no contraindications for whole-body MRI. Additionally, patients with metal implants (e.g., hip replacements) or other source of imaging artefact (e.g., anterior thoracic signal loss, ghosting, and geometric distortion) were not excluded from the study.

Table 1 summarises patient characteristics in the datasets used to develop the signal-based AI-driven software solution. The training set consisted of a single-centre retrospective cohort of 43 patients (**Dataset A**) who underwent pre- and post-treatment WB-DWI. A certified radiologist (5+ years in functional cancer imaging) delineated all metastatic bone disease on the b900 DWI sequence [26] for all scans in **Dataset A**. To assess the repeatability of automated TDV and gADC measurements, we used a cohort of 10 patients (**Dataset B**) who underwent two baseline scans on the same day, using the same scanner and protocol, prior to treatment initiation. For testing, we employed a retrospective multi-centre cohort (**Datasets C**) and a single-centre prospective cohort (**Dataset D**) consisting of 102 and 16 patients, respectively, all of whom underwent pre- and post-treatment WB-DWI. In **Dataset C**, a consultant radiologist (15+ years of experience in whole-body MRI and clinical trials) delineated all metastatic bone lesions on the b900 DWI sequences for a subset of 33 patients (66 scans). Across all datasets, patients underwent follow-up imaging approximately 12 weeks after initiating systemic therapy.

	Pre-treatment	Post-treatment	p-value
<i>Training</i>			
Dataset (A)			
Retrospective single-center cohort 43 patients / 86 WB-DWI scans			
WB-DWI response biomarkers* (manual delineations)			
TDV [mL]	164 [32 - 813]	155 [32 - 927]	0.02
gADC [$\times 10^{-3} \text{ mm}^2/\text{s}$]	0.864 [0.66 - 1.147]	0.917 [0.68 - 1.268]	0.001
<i>Test</i>			
Dataset (B)			
Retrospective single-center cohort 10 patients / 20 WB-DWI scans (Repeatability study)			
Dataset (C)			
Retrospective multi-center cohort 102 patients / 204 WB-DWI scans			
WB-DWI response biomarkers* (manual delineations - 66 scans)			
TDV [mL]	78 [50 - 285]	92 [61 - 325]	<0.001
gADC [$\times 10^{-3} \text{ mm}^2/\text{s}$]	0.926 [0.77 - 1.127]	1.006 [0.808 - 1.267]	<0.001
Response Assessment[†] (constructed <i>reference standard</i>)			
Benefit (responders/stable)	59/102 (57.8%)		
No Benefit (progression)	43/102 (42.2%)		
Dataset (D)			
Prospective single-center cohort 16 patients / 32 WB-DWI scans)			
Response Assessment[†] (constructed <i>reference standard</i>)			
Benefit (responders/stable)	11/16 (68.6%)		
No Benefit (progression)	5/16 (31.4%)		

Table 1. Training and test cohorts used for software development. WB-DWI response biomarkers were derived from expert manual delineations of metastatic bone disease. Response assessment was based on a *construct reference standard* based on clinical assessment, laboratory findings and, all available imaging up to one year after treatment. Pre- and post-treatment TDV and gADC values were compared using the Wilcoxon signed-rank test, with a p-value <0.05 considered statistically significant. †Data are numbers of patients, with percentages in parentheses. *Data are medians, with 1st and 3rd quartiles in parentheses.

2.2 Reference standard for response to treatment

A consensus panel of experienced radiologists and oncologists were used to determine the *construct reference standard* for assessing response to treatment, reviewing all available diagnostic imaging, laboratory test results, and clinical findings up to one year from treatment initiation (see **Table 1**). In **Datasets C and D** APC patients were classified as *Benefit* (responders/stable) or *No Benefit* (progression) from treatment. This dichotomy was designed to evaluate the software for: (i) potential use in clinical trials assessing the therapeutic effects of novel targeted therapies [27]; and (ii) guiding therapy discontinuation in cases of early signs of disease progression.

2.3 Imaging protocol

We used a well-accepted MET-RADS-P compatible [28] whole-body MRI protocol for staging and response assessment of metastatic bone disease including morphological and DWI sequences: sagittal T1/T2 spine, 3D T1w DIXON, T2 HASTE, and DWI with either two (50/900 s/mm²) or three (50/600/900 s/mm²) b-value images [29]. In our study, images were acquired between 2015 and 2023 using a 1.5T scanner (MAGNETOM Aera/Avanto, Siemens Healthcare, Erlangen, Germany). WB-DWI sequences covered 5 or 6 stations, extending either from the skull base to mid-thigh or from the skull vertex to the knees. Each station consisted of 40 slices with a slice thickness of 5mm. WB-DWI was performed using axial 2D single-shot echo-planar imaging with acceleration factor 2 (GRAPPA) and three/four scan trace encoding directions. gADC maps were calculated by fitting a mono-exponential decay model to the b-value images [30], [31]. All MRI parameters related to the acquisition of WB-DWI sequences for each dataset involved in the study are reported in the Supplementary Material (Tables and Figures, **Table S1**).

2.4 Signal-based AI-driven software

Figure 1 shows the main components of the developed software. The software processes pre- and post-treatment whole-body MRI studies as input and generates a structured report as output (see exemplar in Supplementary Material, **Figure S1**). This report includes automated delineations of suspected bone lesions with restricted diffusion properties on DWI (including areas of possible T2 shine through [32]),

along with TDV and gADC measurements and their absolute and percentage changes after treatment. We proposed a two-step approach to enable automated quantification of metastatic bone disease from WB-DWI. *Step one* involves applying our previously validated weakly-supervised deep learning model [33], [34] to generate two key outputs: (i) probability localisation maps for multiple anatomies, including the whole skeleton and spinal canal contents, with the skeleton map isolating bony regions from adjacent soft tissue organs and image background; (ii) a signal-normalised b900 image, generated using the spinal canal mask, to improve inter- and intra-patient variability in signal intensity [35]. For *step two*, we trained a supervised shallow convolutional neural network (CNN) with two input channels derived from step one: (i) the skeleton map and (ii) the signal-normalised b900 image. The single-output channel generates a mask of bony regions with restricted diffusion properties on DWI, as shown in **Figure 1**. The full implementation details for the software pipeline and AI models are available in the Supplementary Material, “Technical Documentation”.

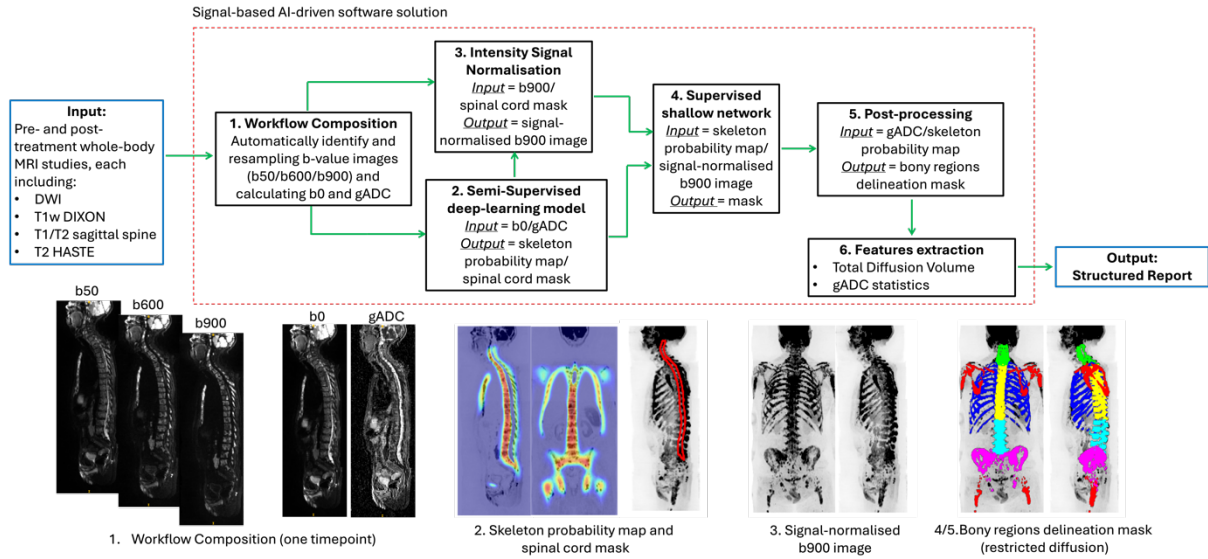


Figure 1. Flow diagram demonstrating the main components of the proposed signal-based AI-driven software solution. The software first analyses pre- and post-treatment whole-body MRI studies as input, automatically identifying and processing WB-DWI sequences at each timepoint separately. A weakly supervised deep learning model facilitates bone disease quantification by generating (i) a skeleton probability map and (ii) spinal canal delineation, which is used to compute a signal-normalised b900 image that enhances contrast between suspected hyperintense bone lesions and normal bone marrow. A supervised shallow CNN is used to generate bone delineation mask, identifying areas indicative of restricted diffusion. This mask is subsequently applied to the corresponding gADC map to: (i) perform post-processing to remove potential false positives by excluding regions with gADC values $< 0.5 \times 10^{-3} \text{ mm}^2/\text{s}$, filtering out signals from normal fatty bone marrow or noise; and (ii) extract TDV and gADC statistics (including median values) for the whole skeleton and individual skeletal regions (limbs, pelvis, thorax, as well as cervical, thoracic and lumbar spinal sub-regions). Once both pre- and post-treatment WB-DWI sequences have been processed, the software generates a structured report with automated delineations of suspected bone lesions and corresponding TDV and gADC measurements, with an average computation time of three minutes for both whole-body MRI studies.

2.5 Software development and testing

2.5.1 Supervised shallow CNN training

We performed 5-fold cross-validation to train the shallow CNN using all WB-DWI scans in **Dataset A**, ensuring that images from the same patient were included in the same training/validation set. For each fold, we calculated the dice score, precision, recall, and average surface distance between automated and expert-defined metastatic bone disease delineations. Additionally, we assessed the relative differences in TDV and median gADC measured from manual and automated methods. TDV was log-transformed (log-TDV) to reduce the scaling effects of errors caused by variability in disease volumes within the patient cohort. The final model was selected based on the cross-validation fold that achieved the highest dice score and the lowest relative error for log-TDV and median gADC.

2.5.2 Accuracy of automated WB-DWI delineation on test datasets

We tested the signal-based AI-driven software solution using 66 WB-DWI scans in **Dataset C**. Automated delineation accuracy was evaluated (i) considering all disease delineations across the skeleton, (ii) for individual skeletal regions, including the limbs, pelvis, lumbar/thoracic/cervical spine, and ribcage, (iii) along with its correlation with manually measured TDV. We reported the same overlap-based metrics and WB-DWI parameters as defined in the cross-validation approach.

2.5.3 Repeatability of automated WB-DWI response biomarkers

Using our software, we generated delineations for all 20 baseline scans in the repeatability cohort (**Dataset B**) and applied them to the corresponding gADC maps to estimate TDV and gADC statistics. We assessed the repeatability of log-TDV as well as mean, median, variance, skewness, and kurtosis for gADC. For all parameters, we reported the coefficient of variation (CoV), repeatability coefficient (RC), within- and between-subject standard deviations (Sw and Sb), and the intraclass correlation coefficient (ICC) [36]. Bland-Altman plots [37] were generated for all parameters and analysed to identify any systematic biases and random errors in measurements of TDV and gADC. Quantitative imaging biomarkers with CoV and RC values below 5% and 15%, respectively, and ICC values above 0.9 will be considered for further investigation in assessing response to treatment.

2.5.4 Accuracy in classifying response to treatment on test datasets

Table 2 shows the proposed REC for quantitatively assessing response to treatment for APC patients based on percentage changes after treatment in TDV (ΔTDV) and median gADC ($\Delta\text{median gADC}$):

1. *Responders*: a significant decrease in ΔTDV ($\leq -40\%$) [38] and/or a significant increase in $\Delta\text{median gADC}$ ($\geq +25\%$) [39], consistent with expected clinical response patterns.
2. *Progression*: If the above criteria are unmet, a significant increase in ΔTDV ($> +40\%$) [22] or an increase in delineated regions compared to the baseline scan.
3. *Stable*: If neither condition is met.

Using our software, we generated automated delineations and extracted TDV and gADC measurements from pre- and post-treatment WB-DWI scans for all patients in **Datasets C** and **D**. The proposed response criteria were applied to these datasets to: (i) test and validate the pre-defined ΔTDV and $\Delta\text{median gADC}$ cutoff values, and (ii) assess accuracy, sensitivity, and specificity by comparing software-based response classification (responder, stable, or progressing) with the *construct reference standard* [40] (Section 2.2).

Post-treatment percentage change in median gADC	Post-treatment percentage change in TDV			
		Significant Increase > +40% or ≥ +10 ROIs (> 1mL) or ≥ +6 ROIs (> 3mL)	No change	Significant Decrease ≤ -40%
	Significant Increase ≥ +25%	Check auto delineations or date of baseline MRI in relation to treatment initiation	<i>Benefit - Responder</i> T2-shine through	<i>Benefit - Responder</i> tumor cell death results in initial increased of water diffusivity
	No change	<i>No Benefit - Progression</i> An increase in the geographic spread of the same type of tumor, along with a higher density of tumor cells	<i>Benefit - Stable</i> Slight alteration in tumor cellularity, minor progression and/or minor response	<i>Benefit - Responder</i> ADC measured from normal bone marrow / areas of scarring, minor areas of non-responding disease
	Decrease	<i>No Benefit - Progression</i> An increase in the geographic spread of the same type of tumor, along with a higher density of tumor cells	<i>Benefit - Stable</i> Slight alteration in tumor cellularity, minor progression and/or minor response	<i>Benefit - Responder</i> ADC measured from normal bone marrow / areas of scarring, minor areas of non-responding disease

Table 2. *Response Evaluation Criteria* (REC) for classifying APC patients as either *Benefit* (responders/stable disease) or *No Benefit* (disease progression) based on automated measurements of TDV and median gADC. This approach accounts for possible combinations of TDV and median gADC changes at follow-up. These changes are based on whole-body DWI sequences (b-value images and gADC maps); and recommended to be used alongside the qualitative assessment by radiologists.

2.6 Statistical Analysis

Values are reported as medians with interquartile ranges (IQRs) for continuous variables. A p -value < 0.05 was considered statistically significant. All analyses were performed using Python 3.9 with Scikit-learn 1.5.0, Statsmodels 0.14.2, and Scipy 1.13.1.

2.6.1 TDV and gADC comparisons

TDV and gADC distributions before and after treatment, based on expert-defined metastatic bone disease delineations, were compared using the Wilcoxon signed-rank test.

2.6.2 Accuracy of automated WB-DWI delineation on test datasets

The correlation between overlap-based metrics (dice score, precision and average surface distance) and manually measured TDV was assessed using the Spearman correlation coefficient (r), interpreted as follows: $r=0.4-0.6$ (moderate), $r=0.6-0.8$ (strong), and $r \geq 0.8$ (very strong).

2.6.3 Repeatability of automated WB-DWI response biomarkers

Repeatability of log-TDV and gADC statistics was evaluated according to QIBA recommendations [41]. A paired two-tailed t-test assessed differences between first and second baseline measurements, with 95% confidence intervals (CIs) calculated for all parameters [36]. If no significant difference was found, a bias of zero (bias=0) was assumed, with the RC equal to the 95% limits of agreement (LoA). ICC values were interpreted as ICC < 0.5 (poor), 0.5-0.75 (moderate), 0.75-0.9 (good), and > 0.9 (excellent).

2.6.4 Accuracy in classifying response to treatment on test datasets

Bootstrapping optimisation was used to identify optimal Δ TDV and Δ median gADC cutoff values and to assess their statistical difference from the pre-defined REC-based thresholds (Section 2.5.4). At each iteration, cutoff pairs were evaluated via a grid search, with binary classifications compared to the *construct reference standard* to identify the combination resulting in the highest Youden's index (above

0.6 indicative of acceptable performance). 95% CIs for the optimal cutoff values were derived from 200 bootstrap iterations on resampled test datasets.

Differences in pre- and post-treatment automated measurements of TDV and median gADC for patients classified as responders or with disease progression were assessed using the Wilcoxon signed-rank test (two-tailed for TDV, one-tailed for median gADC).

Finally, 95% CIs for accuracy, sensitivity, and specificity were calculated using Wilson score interval to assess agreement between the *construct reference standard* and software-based response classification. A diagnostic accuracy of at least 80% was defined as the primary endpoint for evaluating the successful implementation of our software solution.

3. Results

3.1 Patient characteristics

gADC values from expert-defined metastatic bone disease delineations align with literature-reported values for APC patients [42], [43] (**Table 1**). In **Dataset A**, TDV measured 164mL [32-813] pre-treatment and 155mL [32-927] post-treatment, with gADC ranging from 0.66 to $1.147 \times 10^{-3} \text{mm}^2/\text{s}$ and 0.68 to $1.269 \times 10^{-3} \text{mm}^2/\text{s}$, respectively. In **Dataset C**, TDV was 78mL [50–285] pre-treatment and 92mL [61-325] post-treatment, with consistent gADC distributions to **Dataset A**.

3.2 Accuracy of automated WB-DWI delineation on test datasets

The computation time for executing the software pipeline per whole-body MRI scan was 90 seconds on a 2.4 GHz Quad-Core Intel Core i5 processor. **Figure 2** presents the overlap-based metrics between manual and automated delineations, along with the relative error of log-TDV and median gADC across 66 WB-DWI scans (**Dataset C**). A patient-wise dice score of 0.52 [0.34-0.65] was obtained, with most of the error originating from the thorax region, where the score was lower than 0.35. For the upper and lower limbs, the dice score was 0.60 [0.44-0.69] with an average surface distance of 2.96mm [0.75-7.5]. In the pelvis, 0.58 [0.36-0.73] and 3.94mm [0.88-11.8], respectively. For the spine, 0.60 [0.43-0.74] and 1.55mm [0.87-4.55], respectively. The relative differences in log-TDV and median gADC between manual and automated delineations were 8.82% [4.79-22.6] and 4.97% [1.39-16.9], respectively. The highest values for the relative difference in TDV were observed in the thorax, with some variability noted in the lower limbs and cervical spine compared to other skeletal regions. **Figure 3** provides exemplar gADC maps and b900 images from four patients in **Dataset C**, showing both manual and automated delineations of suspected bone lesions.

Nonetheless, we observed moderate-to-strong correlations between automated delineation accuracy and manually measured TDV (**Figure 4**). Increasing TDV correlated positively with dice score ($r=0.55$, $p<0.001$) and precision ($r=0.62$, $p<0.001$), and negatively with average surface distance ($r=-0.70$, $p<0.001$) and relative median gADC difference ($r=-0.54$, $p<0.001$).

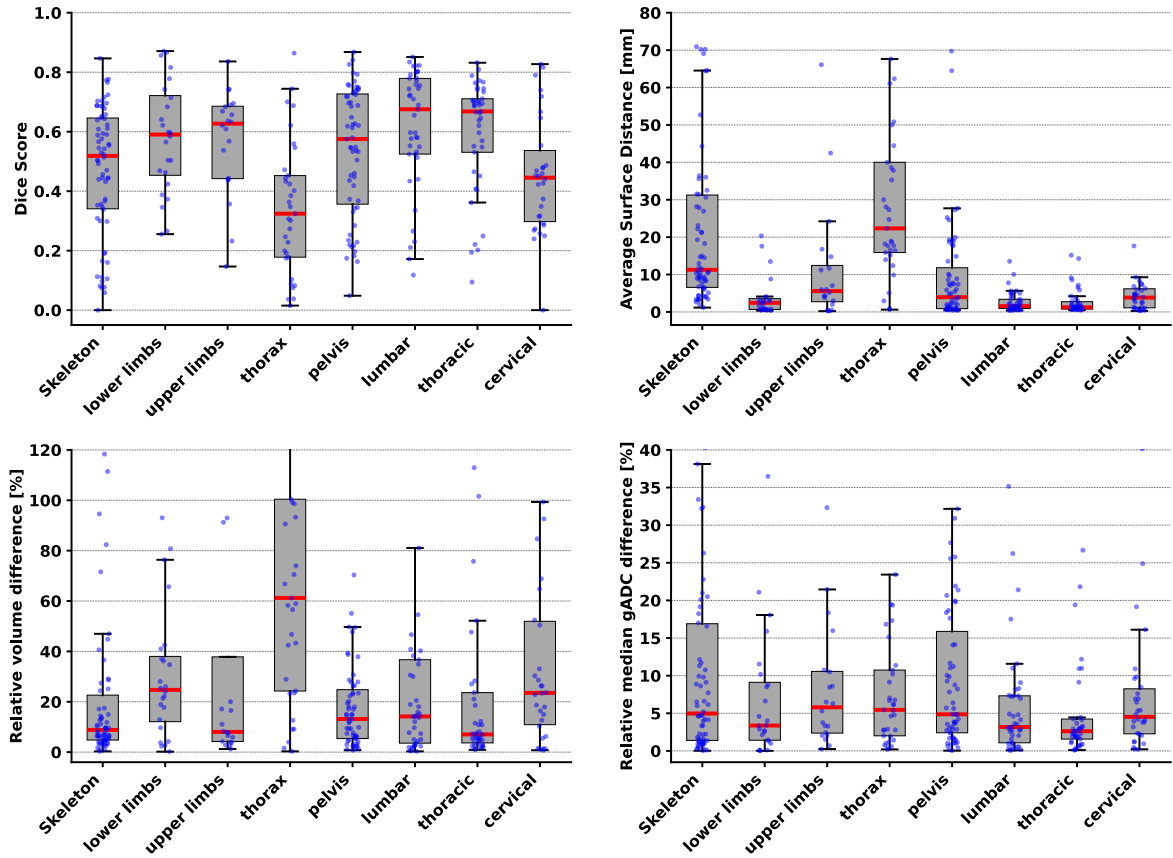
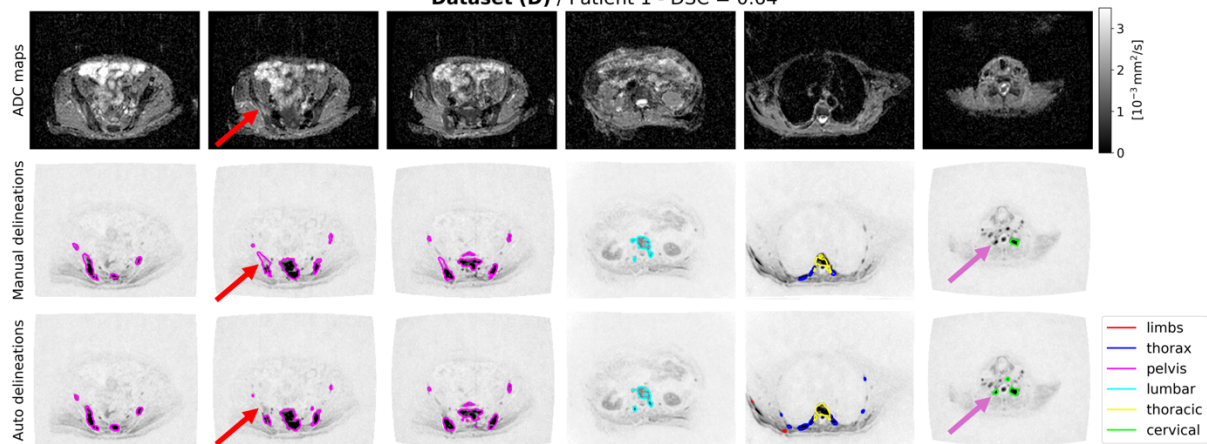
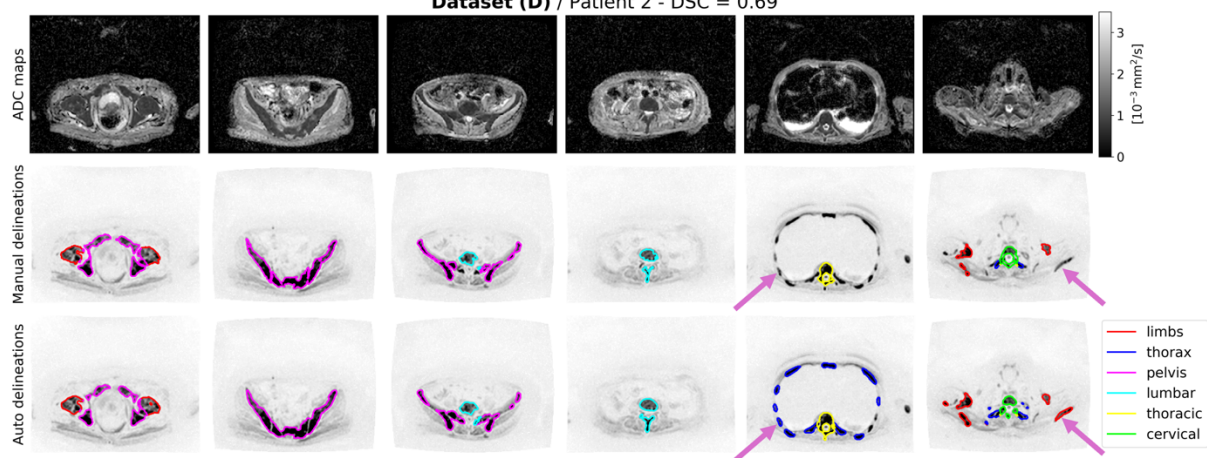


Figure 2. Software accuracy in delineating suspected bone lesions across 66 WB-DWI test datasets (**Dataset C**). Overlap-based metrics (dice score and average surface distance), along with relative differences of volume (log-transformed) and median gADC between automated and expert-defined manual delineations of metastatic bone disease, were assessed for both whole-skeleton delineations and individual skeletal regions (lower/upper limbs, thorax, pelvis, and lumbar/thoracic/cervical spine). Good agreement was observed for lesions detected in the limbs, pelvis, and spine (average dice score of 0.6), while performance was lower in the ribcage (dice score below 0.35).

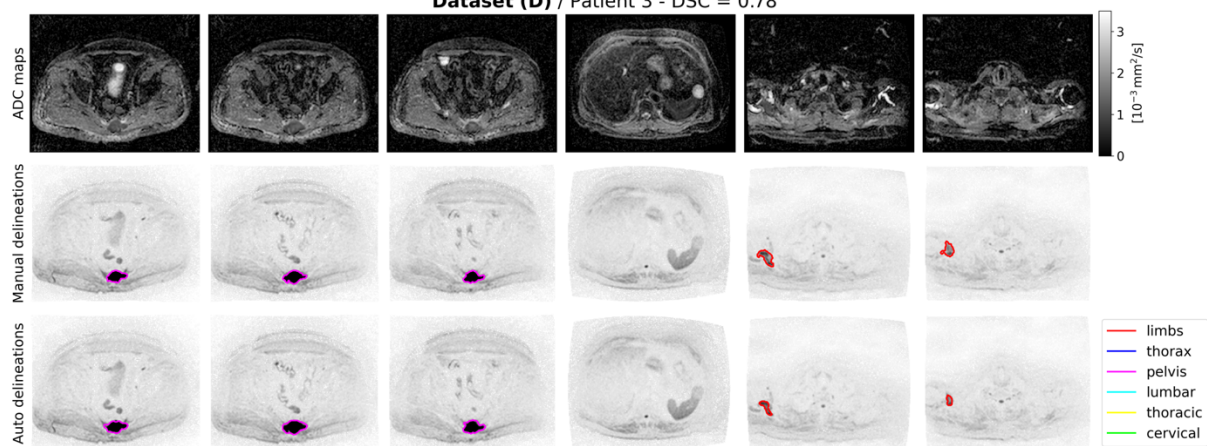
Dataset (D) / Patient 1 - DSC = 0.64



Dataset (D) / Patient 2 - DSC = 0.69



Dataset (D) / Patient 3 - DSC = 0.78



Dataset (D) / Patient 4 - DSC = 0.85

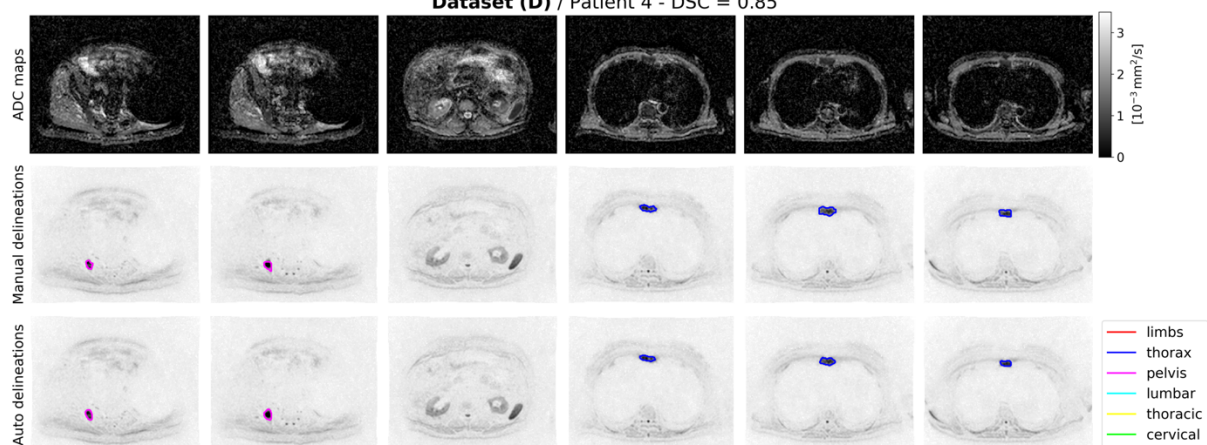


Figure 3. Axial gADC maps and b900 images with superimposed automated and expert-defined manual delineations of metastatic bone lesions from four patients in **Dataset C**. The software detected/delineated suspected bone lesions with high signal intensity on b900 images and low gADC values (typically above $0.5 \times 10^{-3} \text{mm}^2/\text{s}$), while excluding adjacent internal organs and image background. Overall, our solution demonstrated good agreement with the manual method, as indicated by a dice score above 0.64 for these cases. However, false negatives (red arrows) were observed in **Patient 1**, where the manually delineated lesion in the pelvis showed low signal on the b900 image and high gADC values (above $1.4 \times 10^{-3} \text{mm}^2/\text{s}$, likely a treated lesion), suggesting potential inter-reader variability in defining active bone disease. Additionally, the automated mask showed minor imperfections by incorrectly delineating cervical spine nerves (purple arrows). For **Patient 2**, false positives were observed in the ribs and shoulders due to increased normal bone marrow DWI signal (purple arrows). **Patient 3** presented only two metastatic bone lesions, one in the coccyx and one at the top of the shoulders, with suppressed DWI signal from normal bone marrow. Nevertheless, the software-generated delineations showed excellent agreement with the manual method (dice score of 0.78). For **Patient 4**, with a manually measured TDV of 75mL, excellent agreement was observed between manual and automated methods (dice score of 0.85).

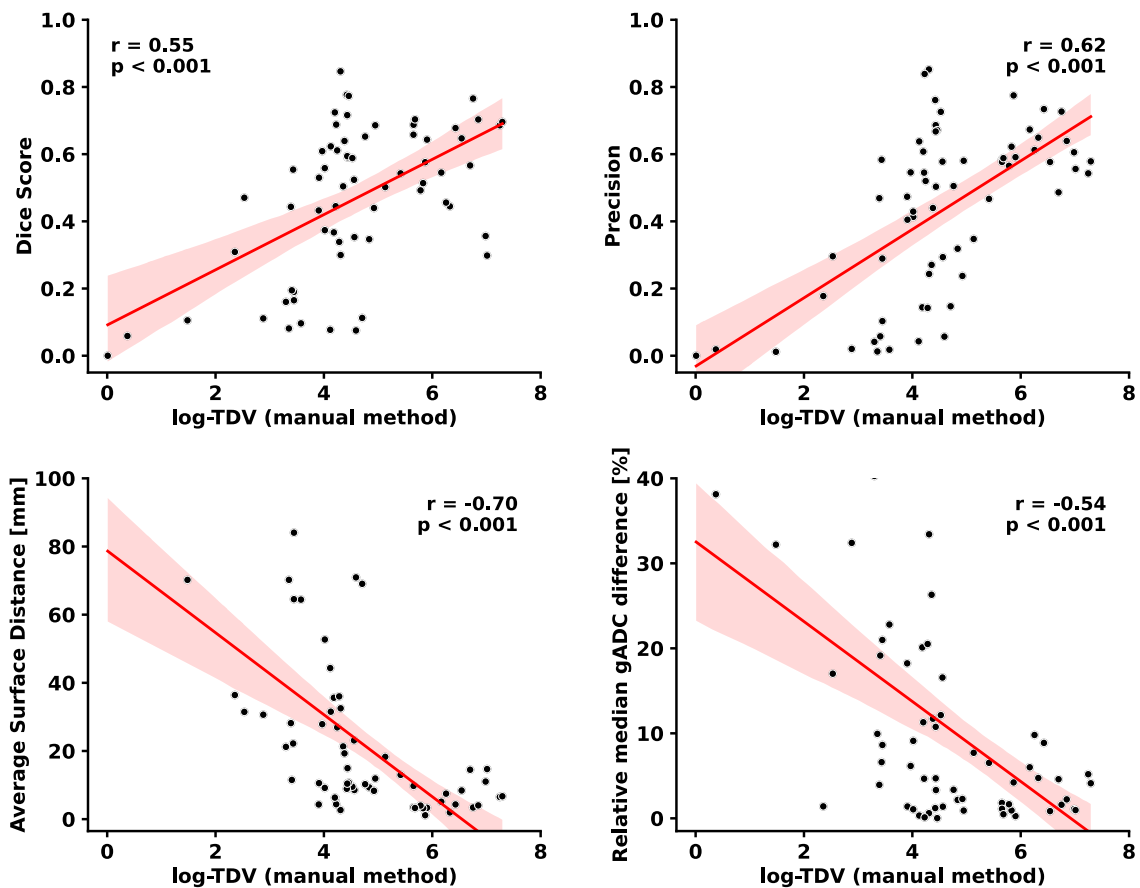


Figure 4. Correlation between software accuracy in delineating suspected bone lesions and manually measured TDV across 66 WB-DWI test datasets (**Dataset C**). Correlations were assessed using Spearman's correlation coefficient (r), with $p < 0.05$ considered statistically significant. Accuracy improved with increasing disease burden. The red line represents the linear fit across all data points, while the shaded red region indicates the standard deviation. For instance, patients with TDV above 55 mL ($\log\text{-TDV}=4$) demonstrated a relative median gADC difference below 12%.

3.3 Repeatability of automated WB-DWI response biomarkers

Among all tested parameters, log-TDV and median gADC demonstrated the best repeatability (see **Table 3**). The CoV for log-TDV and median gADC was 4.57% [95% CIs: 3.19-8.01] and 3.54% [95% CIs: 2.47-6.21], respectively. The RC was 12.66% [95% CIs: 8.84-22.2] for log-TDV and 9.81% [95% CIs: 6.86-17.2] for median gADC. The ICC for both parameters exceeded 0.9, with 95% CIs of 0.81-0.99 for log-TDV and 0.9-0.99 for median gADC. Bland-Altman plots (**Figure S2**) showed no consistent trend suggesting systematic errors in the measurements. The differences in log-TDV and median gADC across all 10 patients fell within the RC, with a bias of -0.0251 ($p=0.828$) for log-TDV and -0.0047 ($p=0.751$) for median gADC, further confirming excellent repeatability. **Figure 5** shows automated delineations for baseline scans of two patients from the repeatability cohort (**Dataset B**).

	CoV (%) [95% CIs]	RC [95% CIs]	RC (%) [95% CIs]	Sw [95% CIs]	Sb [95% CIs]	ICC [95% CIs]
log-TDV	4.57 [3.19 - 8.01]	0.66 [0.46 - 1.16]	12.66 [8.84 - 22.2]	0.24 [0.17 - 0.42]	0.99 [0.69 - 1.73]	0.94 [0.81 - 0.99]
Mean gADC	4.69 [3.28 - 8.83]	0.12 [0.09 - 0.21]	13.0 [9.09 - 22.8]	0.04 [0.03 - 0.08]	0.21 [0.15 - 0.38]	0.96 [0.85 - 0.99]
Median gADC	3.54 [2.47 - 6.21]	0.08 [0.06 - 0.15]	9.81 [6.86 - 17.2]	0.03 [0.02 - 0.05]	0.18 [0.13 - 0.32]	0.97 [0.90 - 0.99]
gADC variance	33.8 [23.6 - 59.4]	0.17 [0.12 - 0.29]	93.8 [65.5 - 164]	0.06 [0.04 - 0.11]	0.14 [0.10 - 0.25]	0.84 [0.52 - 0.96]
gADC skewness	52.0 [36.3 - 91.2]	1.98 [1.38 - 3.48]	144 [101 - 253]	0.71 [0.50 - 1.25]	Not calculable	Not calculable
gADC kurtosis	21.8 [15.3 - 38.3]	3.03 [2.12 - 5.32]	60.5 [42.3 - 106]	1.09 [0.76 - 1.92]	2.76 [1.93 - 4.85]	0.86 [0.57 - 0.96]

Table 3. Summary of repeatability study results for automated delineations along with measurements of TDV and gADC from repeated WB-DWI baseline scans. The table shows the mode estimate for each metric, with 95% confidence intervals indicated in parentheses. The results indicated excellent repeatability for log-TDV and mean/median gADC estimates; however, a trend toward poor reproducibility was noted for higher-order gADC statistics.

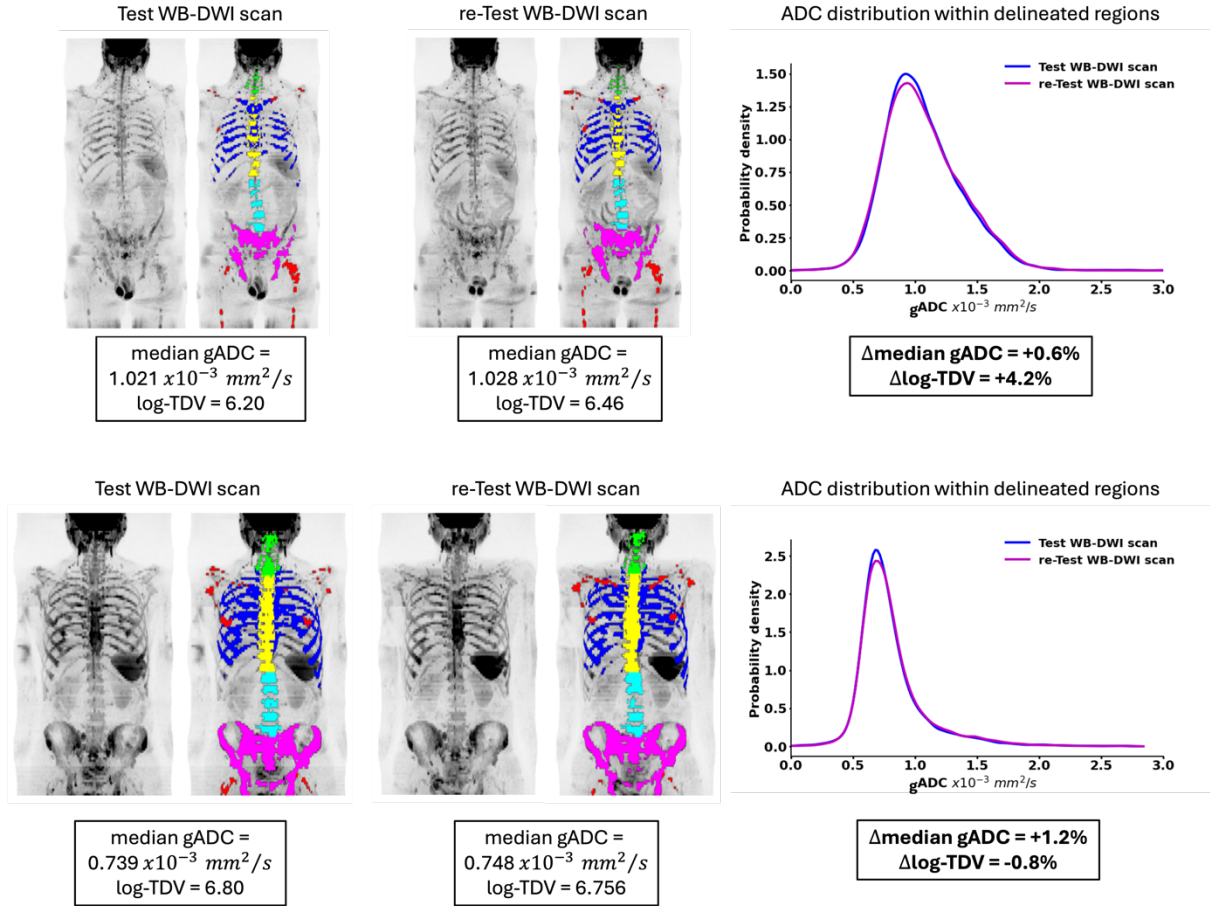


Figure 5. Coronal Maximum-Intensity-Projection (MIP) of signal-normalised b900 images with superimposed automated delineations for two patients from the repeatability cohort (**Dataset B**). The software delineated bony regions with high signal intensity on high b-value images and low gADC values (typically above $0.5 \times 10^{-3} \text{ mm}^2/\text{s}$) within the patient's skeleton, effectively excluding signals from normal bone marrow background, adjacent internal organs, and image background. The delineations were then transferred onto the gADC maps to derive TDV and gADC statistics. log-TDV and median gADC values derived from repeated baseline WB-DWI scans showed minor differences, demonstrating excellent repeatability. The automated delineations are color-coded by skeletal region: upper/lower limbs (red), pelvis (purple), lumbar spine (cyan), thoracic spine (yellow), cervical spine (green), and thorax (blue).

3.4 Accuracy in classifying response to treatment on test datasets

The optimal cutoff values derived from the bootstrapping optimisation approach were $\Delta\text{TDV} \leq -42.6\%$ [95% CIs: -62 to -26.4] and $\Delta\text{median gADC} \geq +28\%$ [95% CIs: $+19$ to $+34$] for responders (Youden's index=0.61 [95% CIs: 0.48-0.73]), and $\Delta\text{TDV} > +36\%$ [95% CIs: $+17$ to $+63$] for disease progression (Youden's index=0.8 [95% CIs: 0.7-0.87]). These cutoff values showed no statistically significant difference in discriminatory performance in our test datasets when compared with the pre-defined REC-based thresholds ($p < 0.05$, Section 2.5.4).

Furthermore, we reported automated TDV and median gADC measurements from pre- and post-treatment scans for responders and patients with disease progression, as classified by the *construct reference standard* (**Figure 6**). Responders (N=43) showed a significant decrease in TDV (from 239mL [85-441] pre-treatment to 131mL [43-300] post-treatment, $p < 0.005$), and a significant increase in median gADC (from $0.815 \times 10^{-3} \text{mm}^2/\text{s}$ [0.709-0.912] pre-treatment to $1.01 \times 10^{-3} \text{mm}^2/\text{s}$ [0.788-1.138] post-treatment, $p < 0.001$). Instead, patients with disease progression (N=48) showed a significant increase in TDV (from 355mL [122-577] pre-treatment to 447mL [256-676] post-treatment, $p < 0.001$). These results align with previous studies, where the same imaging biomarkers at baseline and follow-up were derived from expert-defined delineation of bone lesions in APC patients [22], [38].

Finally, we compared the software-based response classification with the *construct reference standard*. As shown in **Table 4**, our software solution achieved an accuracy of 80.4% (95% CIs: 71.6-87.4), sensitivity of 84.7% (95% CIs: 73-92.1), and specificity of 74.4% (95% CIs: 59.4-85.4) in classifying patients as *Benefit* (responder/stable) or *No Benefit* (progression) from treatment across the retrospective multi-centre cohort (**Dataset C**). In the prospective trial (**Dataset D**), the software achieved an accuracy of 81.2% (95% CIs: 56.4-94.7), with a sensitivity of 81.8% (95% CIs: 50-96.7) and a specificity of 80% (95% CIs: 34.3-99). **Figure 7** presents automated delineations and associated TDV and median gADC measurements for two test cases, one responder and one with disease progression based on the *construct reference standard*, demonstrating the value of non-invasive response imaging biomarkers.

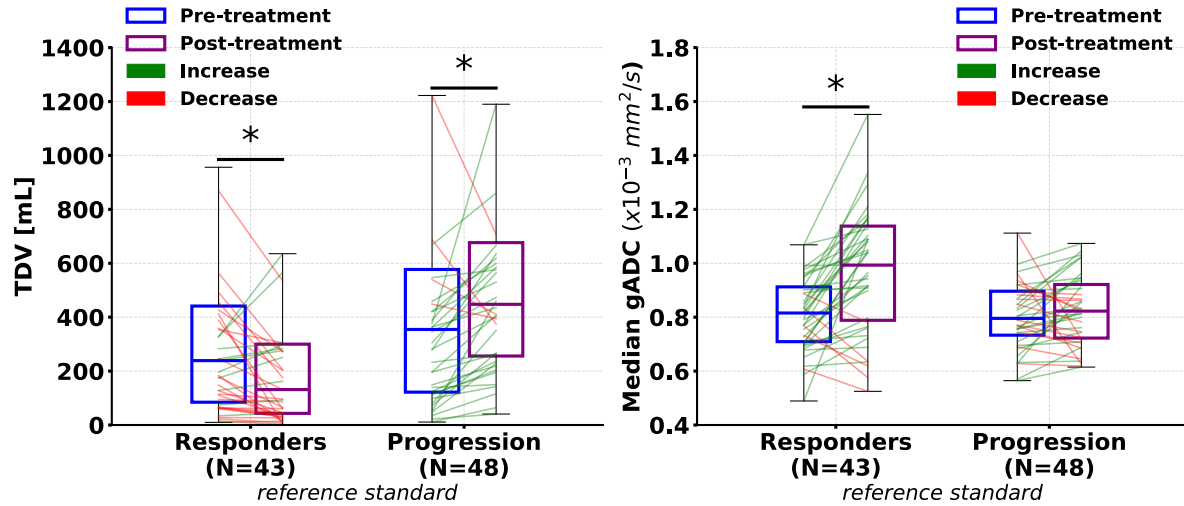


Figure 6. TDV and median gADC values from automated delineations of pre- and post-treatment WB-DWI scans for responders and patients with disease progression, classified according to the *reference standard* constructed by clinicians. This analysis included all patients from test cohorts (**Datasets C and D**). *Significant differences between pre- and post-treatment values are indicated ($p < 0.05$, Wilcoxon signed-rank test: two-tailed for TDV, one-tailed for median gADC).

	Accuracy	Sensitivity	Specificity
Dataset (C) (retrospective multi-center) Benefit (responders/stable) vs. No Benefit (progression)	82/102 (80.4%) [95% CIs: 71.6 - 87.4]	50/59 (84.7%) [95% CIs: 73 - 92.1]	32/43 (74.4%) [95% CIs: 59.4 - 85.4]
Dataset (D) (prospective single-center) Benefit (responders/stable) vs. No Benefit (progression)	13/16 (81.2%) [95% CIs: 56.4 - 94.7]	9/11 (81.8%) [95% CIs: 50% - 96.7%]	4/5 (80%) [95% CIs: 34.3 - 99]
ALL	95/118 (80.5%) [95% CIs: 72.1 - 87]	59/70 (84.3%) [95% CIs: 73.7 - 91.4]	36/48 (75%) [95% CIs: 60.5 - 85.7]

Table 4. Software performance in assessing treatment response in patients with APC. Accuracy, sensitivity, and specificity were calculated by comparing the software-based response assessment to the *reference standard* constructed by clinicians. Accuracy was calculated as (True Positives (TP) + True Negatives (TN)) / (Positives (P) + Negatives (N)), sensitivity TP / P, and specificity TN / N. The overall diagnostic accuracy was 80.5%, with sensitivity and specificity of 84.3 and 75%, respectively.

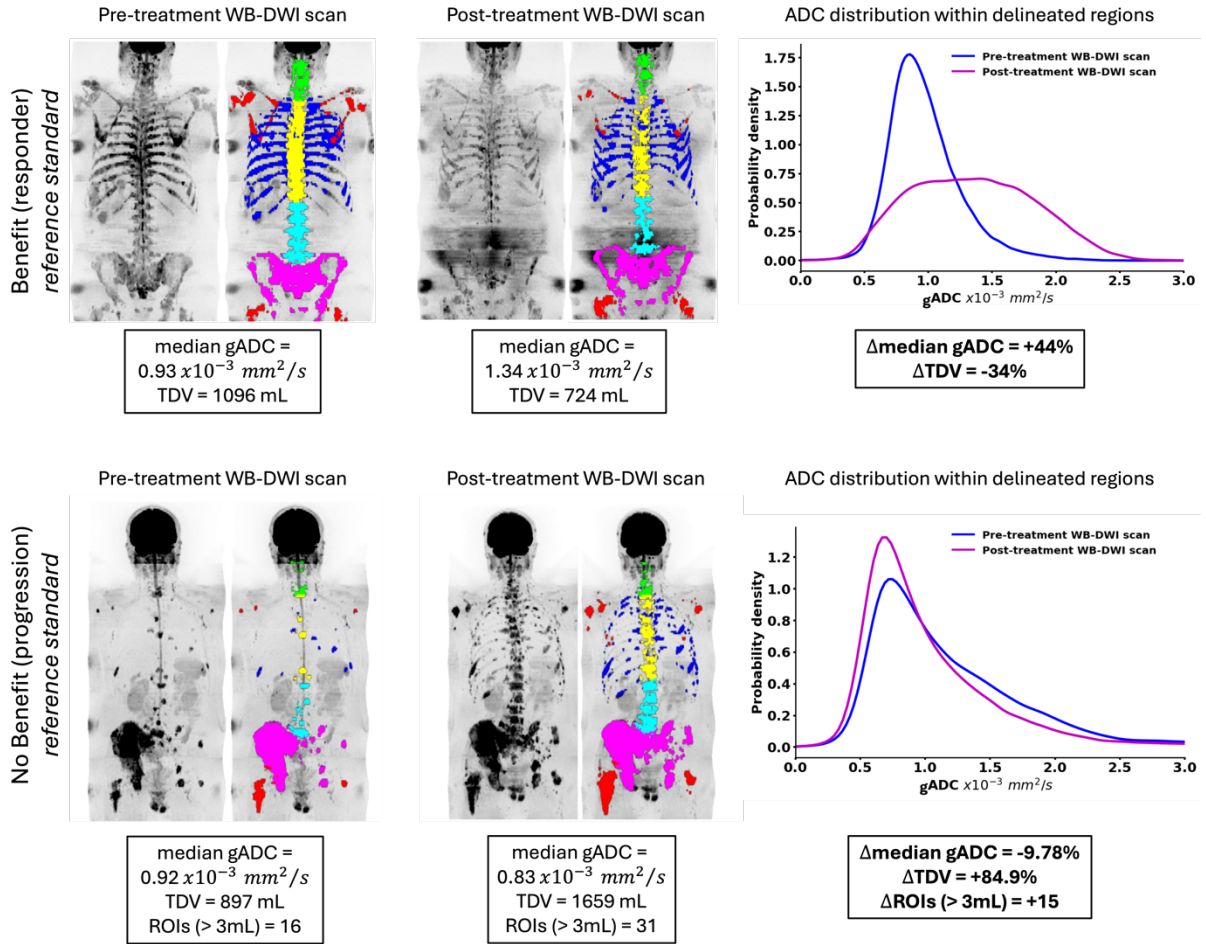


Figure 7. Coronal Maximum-Intensity-Projection (MIP) of signal-normalised b900 pre- and post-treatment images with superimposed automated delineations for two patients in **Dataset D**. The first patient (top row) was classified as a responder, while the second patient (bottom row) was classified as experiencing disease progression, based on the *construct reference standard*. The software delineated bony regions with high signal intensity on high b-value images and low gADC values (typically above $0.5 \times 10^{-3} \text{ mm}^2/\text{s}$) within the patient's skeleton, effectively excluding signals from normal bone marrow, adjacent internal organs, and image background, as expected. The delineations were then transferred onto the gADC map to derive TDV and gADC statistics. Using post-treatment changes in these imaging biomarkers and applying the established REC, the software-based response assessment matched the *reference standard* for both patients. For the first patient, there was a significant increase in the median gADC after treatment, exceeding the cutoff value of +25% (*Benefit*, responder). For the second patient, there was a significant increase in TDV, exceeding the cutoff value of +40% (*No Benefit*, progression), with 15 additional delineated ROIs showing volumes above 3mL between pre- and post-treatment WB-DWI scans. The automated delineations are color-coded by skeletal region: upper/lower limbs (red), pelvis (purple), lumbar spine (cyan), thoracic spine (yellow), cervical spine (green), and thorax (blue).

3. Discussion and Conclusions

We developed and validated a DWI signal-based AI-driven software solution to automatically delineate bony regions with restricted diffusion properties to quantify metastatic bone disease. The software automates the entire process, from image processing of pre- and post-treatment whole-body MRI studies to generating a structured report within three minutes. The report includes TDV and median gADC measurements from delineated regions, aiding response assessment following our developed REC.

Our fully automated method showed good agreement with expert-defined delineations of bone lesions detected in the pelvis and spine, with a dice score of 0.6 [0.41-0.73] and an average surface distance of 2mm. Given that 70% of bone metastases occur in these skeletal regions [3], these results are promising. However, errors were more frequent in the thorax, likely due to coil proximity (causing enhanced signal in anterior and posterior ribs) and geometric/signal distortion from ribs on WB-DWI scans [44]. The software may also incorrectly delineate degenerative disease and nerve roots. Additionally, false positives may occur from normal bone marrow with increased DWI signals (e.g., reactive hyperplasia, inflammatory responses, or treatment effects that increase marrow cellularity and water content). This limitation arises from using a signal-based approach without considering DIXON T1w imaging, where malignant bone lesions show low fat content on calculated rFF maps [45]. However, co-registering whole-body DIXON and DWI sequences remains challenging due to differences in SNR, geometric distortions, and respiratory motion (breath-hold vs. free-breathing) [46]. False negatives may also occur in lesions located at the edges of the inferior pubic rami, shoulders, and clavicles.

Despite these challenges, our method achieved state-of-the-art performance in delineating suspected bone lesions and estimating TDV and median gADC for response evaluation. Ceranka et al. [47] used an nn-UNet model with four-channel input (gADC map, T1w, b900 image, and skeleton mask) to delineate bone metastases on T1w imaging in 27 patients, reporting a patient-wise dice score of 0.33. Their method excluded the thorax and required 180 minutes to generate the final mask. Our software achieved a dice score of 0.6 on 66 test datasets, with higher accuracy in patients with increasing disease

burden (TDV>55 mL; relative median gADC difference <12%), where the interpretation of disease state after treatment may be more challenging, and computation time of just 90 seconds per whole-body MRI study. Colombo et al. [23] employed a semi-automated tool for delineating bone disease in 10 APC patients, reporting an inter-observer dice score of 0.4, a 95% LoA of 10% for mean gADC, and suboptimal TDV reproducibility, with 12-23 minutes required to finalise the mask, depending on reader experience. In contrast, our method showed relative differences of log-TDV and median gADC between manual and automated methods below 5% and 9%, respectively, on test datasets. Furthermore, the repeatability of log-TDV and median gADC was consistent with previous observer repeatability studies using semi-automated delineations of bone lesions. We reported a CoV of 4.57% and 3.54%, a RC of 12.66% and 9.81%, and an ICC of 0.94 and 0.97 for log-TDV and median gADC respectively, compared with CoV and RC values below 7% and 3%, and an ICC above 0.97 for the same WB-DWI biomarkers [48]. Finally, our software demonstrated good agreement with the *construct reference standard* for classifying patients as responders, stable, or with disease progression across 118 test datasets. The overall diagnostic accuracy was 80.5%, exceeding conventional imaging modalities for assessing response to treatment in APC patients [49].

However, there are limitations to our current software. First, the software was tested on WB-DWI scans from a single MRI vendor, which may limit generalisability. Variations in MRI protocols across vendors can impact image quality, leading to decreased SNR, increased geometric distortions, and artifacts [50], potentially reducing the accuracy of automated delineations. Second, the current version of our software does not make use of the relative fat fraction to further refine the classification of disease and non-disease. Disease delineation based on DWI signal intensity alone can lead to false positive results (e.g. due to T2 shine through from treated lesions, reactive cellular marrow or degenerative changes). We are currently developing a model that will include the use of relative fat fraction to improve diagnostic performance. Third, this study is set up with an imperfect, although the best available gold standard regarding lesion delineation, as even expert reader bone disease delineations show significant inter-reader variability and are subject to interpretation. Last, the current software version does not account for disease to lymph nodes and/or soft tissue organs (e.g., liver metastases), which may co-exist within

patients [51]. However, the evaluation of treatment response in lymph nodes and soft tissue is well-established and there are already software available to provide accurate and objective quantification of disease at these sites.

In conclusion, our automated software solution can quickly generate accurate and reproducible delineations of bony regions with restricted diffusion properties on DWI, thus providing estimations of TDV and gADC of bone disease for tracking treatment response in patients with APC. A prospective evaluation of our software is ongoing in a multi-centre national trial. The trial aims to demonstrate the value of our software output in directing treatment decisions, thereby improving patient outcomes using WB-DWI instead of conventional imaging techniques.

4. Supplementary Material – Tables and Figures

	Dataset (A) (43 patients/ 86 WB-DWI scans)		Dataset (B) (10 patients/ 20 WB-DWI scans)	Dataset (C) (102 patients/ 204 WB-DWI scans)		Dataset (D) (16 patients/ 32 WB-DWI scans)
Dataset Split	Retrospective single-center cohort (Training, 5-fold cross-validation)		Retrospective single-center cohort (Repeatability study)	Retrospective multi-center cohort (Test)		Prospective single-center cohort (Test)
MR scanner	1.5T Siemens Aera		1.5T Siemens Aera	1.5T Siemens Aera/Avanto		1.5T Siemens Aera
Sequence	Diffusion-Weighted SS-EPI		Diffusion-Weighted SS-EPI	Diffusion-Weighted SS-EPI		Diffusion-Weighted SS-EPI
Acquisition plane	Axial		Axial	Axial		Axial
Breathing mode	Free breathing		Free breathing	Free breathing		Free breathing
b-values [s/mm^2]	b50/b900 (N = 4)	b50/b600/b900 (N = 39)	b50/b600/b900 (N = 10)	b50/b900 (N = 38)	b50/b600/b900 (N = 64)	b50/b600/b900 (N = 16)
Number of averages per b-value	(3, 5)	[(2, 2, 4) - (3, 3, 5)]	(3, 3, 5)	(4, 4)	[(3, 3, 5) - (3, 6, 6)]	(3, 6, 6)
Reconstructed resolution [mm^2]	[1.56 x 1.56 – 1.68 x 1.68]		[1.56 x 1.56 – 3.12 x 3.12]	[1.4 x 1.4 – 3.12 x 3.12]		3.21 x 3.21
Slice thickness [mm]	5		6	[5 – 6]		5
Repetition time [ms]	[6150 – 12700]		11300	[5490 – 12003]		6320
Echo time [ms]	[60 – 79]		69	[69 – 73]		76
Inversion time (STIR fat suppression) [ms]	180		180	180		180
Flip angle [°]	90		90	[90 – 180]		90
Reconstructed matrix [mm]	[98 x 128 – 256 x 256]		208 x 256	[130 x 160 – 208 x 256]		108 x 134
Receive bandwidth [Hz/Px]	[1955 – 2330]		1955	1955		2195

Table S1. Scanning protocol and MRI parameters for all WB-DWI datasets investigated in our study. Minimum and maximum values are displayed in parenthesis.

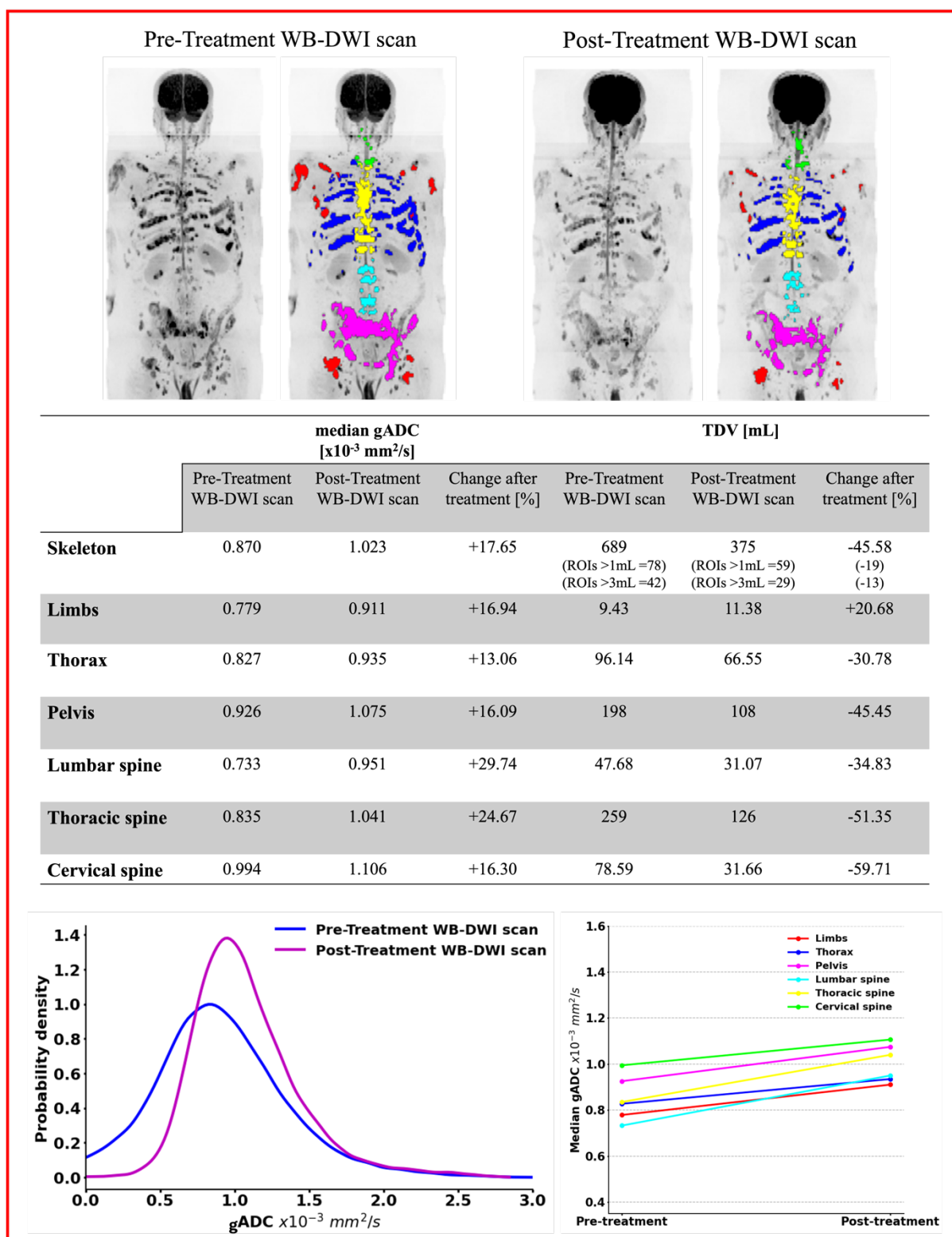


Figure S1. Automated structured report generated from the AI-driven software solution after processing pre- and post-treatment WB-DWI scans.

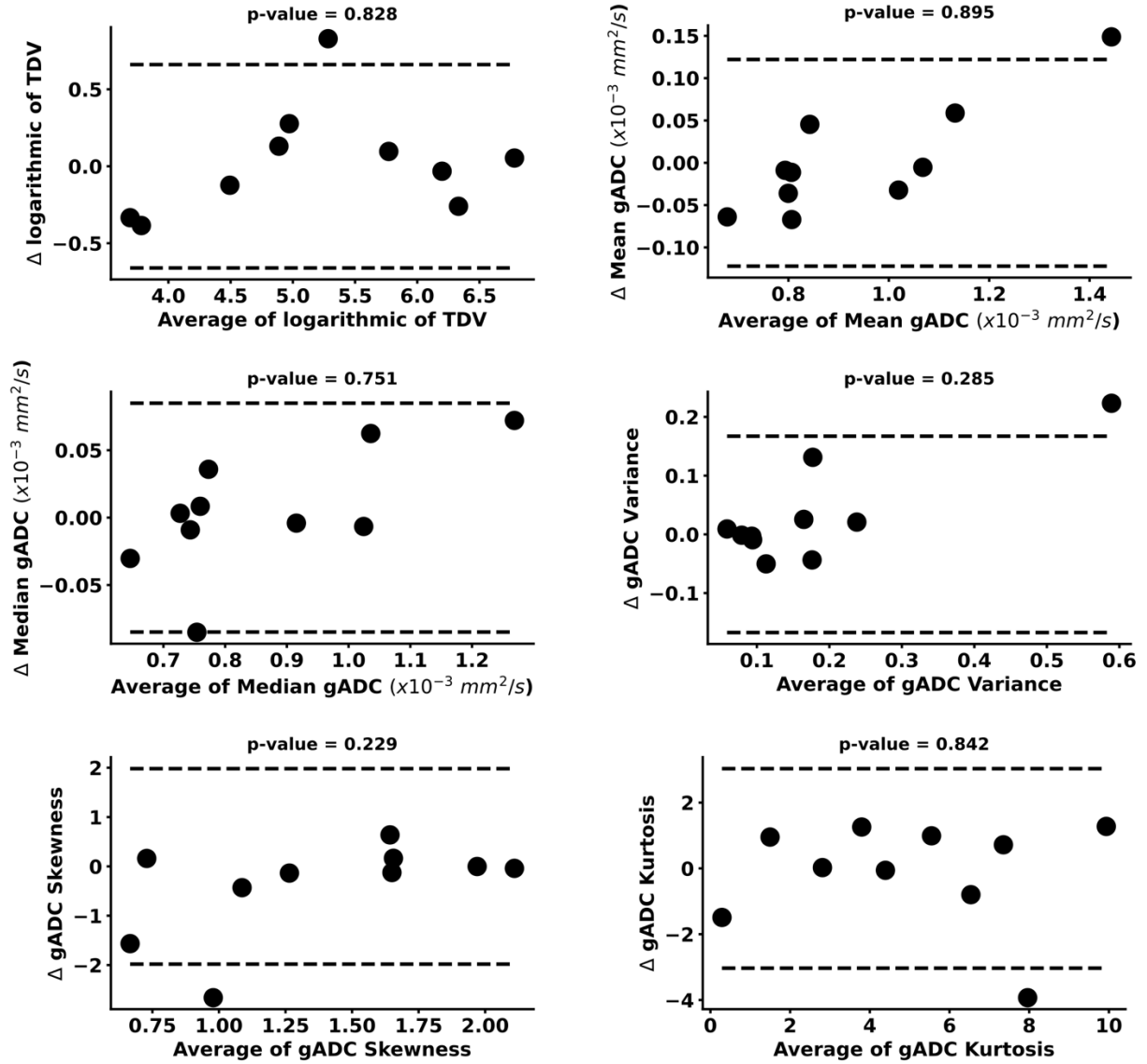


Figure S2. Bland-Altman plots for repeatability measurements of log-TDV and gADC statistics derived from automated delineations of 10 APC patients who underwent two WB-DWI baseline scans. The plots display the limits of agreement (LoA, dashed black lines) and the results of a two-tailed paired t-test to assess any correlation between the differences in repeated measurements of each parameter (vertical axis) and their average values (horizontal axis).

5. Supplementary Material – Technical Documentation

5.1 Workflow Composition

The software solution automatically identifies the DWIs based on key DICOM tags and the availability of b-values in the metadata from the WB-MRI study. To successfully trigger subsequent steps in the software pipeline, the WB-MRI study must include at least two b-value series, which are then assembled from the b-value station data to create whole-body images. If resampling is required, the lower b-value images, $b=50 \text{ s/mm}^2$ (b50) and $b=600 \text{ s/mm}^2$ (if present), are aligned with the grid of the highest b-value image (b900). Additional steps may be necessary to correct for artifacts and mismatches in the acquired data, ensuring consistency in spatial resolution, signal-to-noise ratio (SNR), and reliable gADC values. Finally, the gADC map and intercept image (S_0) at $b=0 \text{ s/mm}^2$ are calculated by fitting a mono-exponential decay model to the generated whole-body b-value images [30], [31].

5.2 WB-DWI body region probability maps

We hypothesise that a logical first step in developing an automated tool for delineating suspected bone lesions is generating a skeleton mask. To support this, we previously developed and validated a weakly-supervised deep learning model that localises and delineates skeletal regions, adjacent internal organs (liver, spleen, kidneys, and urinary bladder), and the spinal canal contents (spinal cord along with the surrounding cerebrospinal fluid, CSF) from WB-DWI scans [34]. Our algorithm, based on a 3D patch-based Residual U-Net (Res U-Net) architecture, was trained using 532 WB-DWI scans paired with examples of “soft-labels” (non-binary segmentations) generated through a computationally intensive atlas-based segmentation approach [33]. The network employs a 2-channel input: (i) the calculated gADC map and (ii) the S_0 image, and a multi-channel output that generates probability maps for seven skeletal regions (legs, pelvis, lumbar/thoracic/cervical spine, ribcage, and arms/shoulders), four adjacent internal organs (liver, spleen, urinary bladder, and kidneys), and the spinal canal. The inference time of the weakly-supervised model is on average 25 seconds on a 2.4 GHz Quad-Core Intel Core i5 processor. The spinal canal delineations are then used to implement an intensity signal normalisation method for WB-DWI scans, while the skeleton probability map guides a second model in delineating

ROIs with abnormal WB-DWI signal intensity within the patient's skeleton. Additionally, the internal organ delineations are used to remove false positives during a post-processing step.

5.3 WB-DWI intensity signal normalisation

WB-DWI scans show inter- and intra-patient variability in signal intensity, which can hinder accurate quantification of bone disease and the tracking of changes over follow-up scans. To address this challenge, we implemented a method for inter-station and inter-scan signal standardisation on WB-DWI scans, employing the spinal cord and surrounding CSF delineations obtained from the weakly-supervised Res U-Net model [35]. Our method harmonises signal intensity on computed b900 images (cDWIs) [30] through two stages: (i) normalisation of signal between imaging stations within each patient through histogram equalisation of slices acquired on either side of the station gap, and (ii) inter-scan normalisation through histogram equalisation of the signal derived within segmented spinal cord and CSF regions. The computation time for generating a signal-normalised b900 image is on average 10 seconds on a 2.4 GHz Quad-Core Intel Core i5 processor.

5.4 Supervised shallow convolutional neural network (CNN)

The derived skeleton probability maps and signal-normalised b900 images accelerate the training and inference times of an explainable machine learning model designed to automatically delineate suspected bone lesions from WB-DWI scans. Compared to threshold-based methods that generate coarse masks, the machine learning model predicts smoother, more focused boundaries, reducing noise and artifacts for higher-quality segmentations. To achieve this, we trained a supervised convolutional shallow network with three hidden layers, using two-channel inputs: (i) the derived skeleton probability map and (ii) the b900 signal-normalised image. The hidden layers employed 16, 32, and 64 filters, respectively, with a 3x3 kernel size, batch normalization, a 0.2 dropout rate, and ReLU activation. The final layer used a sigmoid activation function. Adam optimization (learning rate 10^{-3}) minimised a dice and cross-entropy-based loss function over 150 epochs, with a batch size of 16 and a patch size of 64x64x64. All input images were interpolated to a 256x256 matrix with a 1.6x1.6 mm resolution. The output from the shallow CCN is a mask with ROIs that show restricted diffusion properties (high signal

intensity on normalised b900 images compared to normal bone marrow background) throughout the patient 'skeleton.

5.5 Post-processing step

A post-processing routine was implemented to reduce false positives observed in the generated mask from the supervised shallow CNN. First, the mask was processed using the connected components algorithm, enabling the manipulation of individual ROIs. Each ROI was then transferred to the calculated gADC map, and any ROIs showing 65% or more of their voxels with gADC values below $0.5 \times 10^{-3} \text{ mm}^2/\text{s}$ (typically visualised as WB-DWI signal from fatty bone marrow or noise) [43] were removed from the final segmentation mask. Additionally, ROIs overlapping with the derived internal organ delineations were excluded.

5.6 Features Extraction

After the post-processing step, the final segmentation mask was multiplied by the skeletal regions mask and transferred to the calculated gADC map to extract the WB-DWI response biomarkers. We report the TDV and median gADC for the whole skeleton (global measurements) as well as for individual skeletal regions (lower/upper limbs, pelvis, thorax, lumbar/thoracic/cervical spine).

5.7 Prototype Development and C++ Implementation

We developed a prototype of the software solution in Python v.3.9, using SimpleITK v.2.2.1, NumPy v.1.24.3, PyTorch v.2.0.1, and MONAI v.0.9.1. The machine learning models were implemented using PyTorch v.2.3.0+cu118 and trained on an NVIDIA Quadro RTX 5000 GPU. Building on the Python prototype, we developed a C++ software solution using Boost v.1.76, ITK v.4.13.1, Armadillo v.11.4.0. The pre-trained Torch models were converted to ONNX v.1.13.1 for inference in the C++ environment. Our objective was to achieve an average dice score of at least 0.95 by comparing generated masks from the Python prototype and the C++ implementation of the automated tool using all scans in our datasets. We met this condition, and consequently, all results presented in this study are based on the C++ implementation of the software, rigorously tested following a Quality Management System (QMS).

- **Author Contributions**

Conceptualization, A.C., M.D.B. and D.-M.K.; methodology, A.C. and M.D.B.; software, A.C. and R.H.; validation, A.C., R.H., M.D.B., N.T., and D.-M.K.; formal analysis, A.C.; resources, R.D., C.M., N.T., and D.-M.K.; data curation, A.C. and R.H.; writing-original draft preparation, A.C.; writing-review and editing, A.C., R.H., A.R., N.P., F.Z., L.D., F.C., R.D., A.D., C.M., N.T., M.D.B. and D.-M.K.; supervision, M.D.B. and D.-M.K.; project administration, A.R.; funding acquisition, M.D.B. and D.-M.K. All authors have read and agreed to the published version of the manuscript.

- **Funding**

This project is funded by the NIHR Invention for Innovation award (Advanced computer diagnostics for whole body magnetic resonance imaging to improve management of patients with metastatic bone cancer II-LA-0216-20007).

- **Acknowledgments**

This study represents independent research funded by the National Institute for Health and Care Research (NIHR) Biomedical Research Centre at The Royal Marsden NHS Foundation Trust and The Institute of Cancer Research, London, and by the Royal Marsden Cancer Charity and Cancer Research UK (CRUK) National Cancer Imaging Trials Accelerator (NCITA), and is funded by the NIHR Invention for Innovation award (Advanced computer diagnostics for whole body magnetic resonance imaging to improve management of patients with metastatic bone cancer II-LA-0216-20007). The views expressed are those of the author(s) and not necessarily those of the NIHR or the Department of Health and Social Care. This work uses data provided by patients and collected by the NHS as part of their care and support.

The authors would also like to acknowledge Mint Medical®.

- **Informed Consent Statement**

Patient consent was waived; study was conducted with retrospective and prospective data and researchers only had access to de-identified data. The retrospective data were analysed as part of a service evaluation (SE696), while the prospective data were collected under the WISE study, registered with ClinicalTrials.gov, ID: NCT04117594).

- **Data Availability Statement**

Data can be shared upon request from the authors. However, this is subject to the establishment of an appropriate data-sharing agreement, given the sensitive nature of patient information involved.

- **Conflicts of interest**

A.C., R.H., and M.D.B. have submitted a patent to the UK Intellectual Property Office regarding the work described in this manuscript.

References

- [1] L. Bubendorf *et al.*, “Metastatic patterns of prostate cancer: An autopsy study of 1,589 patients,” *Hum Pathol*, vol. 31, no. 5, pp. 578–583, 2000
- [2] F. Macedo *et al.*, “Bone Metastases: An Overview,” *Oncol Rev*, vol. 11, no. 1, 2017
- [3] R. E. Coleman, “Clinical Features of Metastatic Bone Disease and Risk of Skeletal Morbidity,” *Clinical Cancer Research*, vol. 12, no. 20 PART 2, pp. 6243–6250, 2006
- [4] C. Parker *et al.*, “Alpha Emitter Radium-223 and Survival in Metastatic Prostate Cancer,” *n engl j med*, vol. 369, pp. 213–236, 2013
- [5] J. Sturge, M. P. Caley, J. Waxman, J. Sturge, M. P. Caley, and J. Waxman, “Bone metastasis in prostate cancer: emerging therapeutic strategies,” *Nature Publishing Group*, vol. 8, pp. 357–368, 2011
- [6] I. F. Tannock *et al.*, “Docetaxel plus Prednisone or Mitoxantrone plus Prednisone for Advanced Prostate Cancer,” *N Engl J Med*, vol. 351, no. 15, pp. 1502–1512, 2004
- [7] H. I. Scher *et al.*, “Trial design and objectives for castration-resistant prostate cancer: Updated recommendations from the prostate cancer clinical trials working group 3,” *Journal of Clinical Oncology*, vol. 34, no. 12, pp. 1402–1418, 2016
- [8] E. A. Eisenhauer *et al.*, “New response evaluation criteria in solid tumours: Revised RECIST guideline (version 1.1),” *Eur J Cancer*, vol. 45, no. 2, pp. 228–247, 2009
- [9] H. L. Yang, T. Liu, X. M. Wang, Y. Xu, and S. M. Deng, “Diagnosis of bone metastases: A meta-analysis comparing 18FDG PET, CT, MRI and bone scintigraphy,” *Eur Radiol*, vol. 21, no. 12, pp. 2604–2617, 2011
- [10] E. Balliu *et al.*, “Comparative study of whole-body MRI and bone scintigraphy for the detection of bone metastases,” *Clin Radiol*, vol. 65, no. 12, pp. 989–996, 2010
- [11] G. Shen, H. Deng, S. Hu, and Z. Jia, “Comparison of choline-PET/CT, MRI, SPECT, and bone scintigraphy in the diagnosis of bone metastases in patients with prostate cancer: a meta-analysis,” *Skeletal Radiol*, vol. 43, no. 11, pp. 1503–1513, 2014
- [12] E. Dyrberg *et al.*, “68 Ga-PSMA-PET/CT in comparison with 18 F-fluoride-PET/CT and whole-body MRI for the detection of bone metastases in patients with prostate cancer: a prospective diagnostic accuracy study,” *Eur Radiol*, vol. 29, no. 3, pp. 1221–1230, 2019
- [13] A. Gafita *et al.*, “Response Evaluation Criteria in PSMA PET/CT (RECIP 1.0) in Metastatic Castration-resistant Prostate Cancer,” *Radiology*, vol. 308, no. 1, 2023
- [14] S. Vaz, B. Hadaschik, M. Gabriel, K. Herrmann, M. Eiber, and D. Costa, “Influence of androgen deprivation therapy on PSMA expression and PSMA-ligand PET imaging of prostate cancer patients,” *Eur J Nucl Med Mol Imaging*, vol. 47, no. 1, pp. 9–15, 2020
- [15] A. R. Padhani *et al.*, “Rationale for Modernising Imaging in Advanced Prostate Cancer,” *Eur Urol Focus*, vol. 3, no. 2–3, pp. 223–239, 2017
- [16] R. Perez-lopez, D. N. Rodrigues, I. Figueiredo, J. Mateo, and D. J. Collins, “Multiparametric Magnetic Resonance Imaging of Prostate Cancer Bone Disease Correlation with Bone Biopsy Histological and Molecular Features,” *Invest Radiol*, vol. 53, no. 2, 2018
- [17] D. M. Koh *et al.*, “Whole-body diffusion-weighted mri: Tips, tricks, and pitfalls,” *American Journal of Roentgenology*, vol. 199, no. 2, pp. 252–262, 2012

- [18] A. R. Padhani, K. Van Ree, D. J. Collins, S. D'Sa, and A. Makris, "Assessing the relation between bone marrow signal intensity and apparent diffusion coefficient in diffusion-weighted MRI," *American Journal of Roentgenology*, vol. 200, no. 1, pp. 163–170, 2013
- [19] R. Perez-Lopez *et al.*, "Imaging Diagnosis and Follow-up of Advanced Prostate Cancer: Clinical Perspectives and State of the Art," *Radiology*, vol. 292, no. 2, pp. 273–286, 2019
- [20] A. R. Padhani, A. Makris, P. Gall, D. J. Collins, N. Tunariu, and J. S. De Bono, "Therapy monitoring of skeletal metastases with whole-body diffusion MRI," *Journal of Magnetic Resonance Imaging*, vol. 39, no. 5, pp. 1049–1078, 2014
- [21] A. R. Padhani, D. M. Koh, and D. J. Collins, "Whole-body diffusion-weighted MR imaging in cancer: Current status and research directions," *Radiology*, vol. 261, no. 3, pp. 700–718, 2011
- [22] M. D. Blackledge *et al.*, "Assessment of treatment response by total tumor volume and global apparent diffusion coefficient using diffusion-weighted MRI in patients with metastatic bone disease: A feasibility study," *PLoS One*, vol. 9, no. 4, pp. 1–8, 2014
- [23] A. Colombo *et al.*, "Semi-automated segmentation of bone metastases from whole-body mri: Reproducibility of apparent diffusion coefficient measurements," *Diagnostics*, vol. 11, no. 3, 2021
- [24] R. Grimm and A. R. Padhani, "Whole-body Diffusion-weighted MR Image Analysis with syngo.via Frontier MR Total Tumor Load," *MAGNETOM Flash*, vol. 68, no. 2, pp. 73–75, 2017
- [25] Y. Kohada *et al.*, "Novel quantitative software for automatically excluding red bone marrow on whole-body magnetic resonance imaging in patients with metastatic prostate cancer: A pilot study," *International Journal of Urology*, vol. 30, no. 4, pp. 356–364, 2023
- [26] R. Donners *et al.*, "Inter- and Intra-Patient Repeatability of Radiomic Features from Multiparametric Whole-Body MRI in Patients with Metastatic Prostate Cancer," *Cancers (Basel)*, vol. 16, no. 9, p. 1647, 2024
- [27] J. Mateo *et al.*, "Olaparib in patients with metastatic castration-resistant prostate cancer with DNA repair gene aberrations (TOPARP-B): a multicentre, open-label, randomised, phase 2 trial," *Lancet Oncology*, vol. 21, no. 1, pp. 162–174, 2020
- [28] A. R. Padhani *et al.*, "METastasis Reporting and Data System for Prostate Cancer: Practical Guidelines for Acquisition, Interpretation, and Reporting of Whole-body Magnetic Resonance Imaging-based Evaluations of Multiorgan Involvement in Advanced Prostate Cancer," *Eur Urol*, vol. 71, no. 1, pp. 81–92, 2017
- [29] J. M. Winfield, M. D. Blackledge, N. Tunariu, D. M. Koh, and C. Messiou, "Whole-body MRI: a practical guide for imaging patients with malignant bone disease," *Clin Radiol*, vol. 76, no. 10, pp. 715–727, 2021
- [30] M. D. Blackledge *et al.*, "Computed Diffusion-weighted MR Imaging May Improve Tumor Detection," *Radiology*, vol. 261, no. 2, pp. 573–81, 2011
- [31] M. D. Blackledge *et al.*, "Noise-Corrected, Exponentially Weighted, Diffusion-Weighted MRI (niceDWI) Improves Image Signal Uniformity in Whole-Body Imaging of Metastatic Prostate Cancer," *Front Oncol*, vol. 10, pp. 1–12, 2020
- [32] D. M. Koh and D. J. Collins, "Diffusion-weighted MRI in the body: Applications and challenges in oncology," *American Journal of Roentgenology*, vol. 188, no. 6, pp. 1622–1635, 2007
- [33] A. Candito *et al.*, "Deep learning assisted atlas-based delineation of the skeleton from Whole-Body Diffusion Weighted MRI in patients with malignant bone disease," *Biomed Signal Process Control*, vol. 92, p. 106099, 2024
- [34] A. Candito *et al.*, "A weakly-supervised deep learning model for fast localisation and delineation of the skeleton, internal organs, and spinal canal on Whole-Body Diffusion-Weighted MRI (WB-DWI)," 2025

- [35] A. Candito *et al.*, “Deep Learning for Delineation of the Spinal Canal in Whole-Body Diffusion-Weighted Imaging: Normalising Inter- and Intra-Patient Intensity Signal in Multi-Centre Datasets,” *Bioengineering*, vol. 11, no. 2, p. 130, 2024
- [36] J. M. Winfield *et al.*, “Extracranial Soft-Tissue Tumors: Repeatability of Apparent Diffusion Coefficient Estimates from Diffusion-weighted MR Imaging,” *Radiology*, vol. 284, no. 1, 2017
- [37] J. M. Bland and D. G. Altman, “Statistical methods for assessing agreement between two methods of clinical measurement,” *Int J Nurs Stud*, vol. 47, no. 8, pp. 931–936, 2010
- [38] R. Perez-Lopez *et al.*, “Diffusion-weighted imaging as a treatment response biomarker for evaluating bone metastases in prostate cancer: A pilot study,” *Radiology*, vol. 283, no. 1, pp. 168–177, 2017
- [39] C. Parker *et al.*, “Radium-223 in metastatic castration-resistant prostate cancer: whole-body diffusion-weighted magnetic resonance imaging scanning to assess response,” *Cancer Spectrum*, vol. 7, no. 6, 2023
- [40] A. Rutjes, J. B. Reitsma, A. Coomarasamy, K. S. Khan, and P. Bossuyt, “Evaluation of diagnostic tests when there is no gold standard. A review of methods,” *Health Technol Assess (Rockv)*, vol. 11, no. 50, 2007
- [41] D. L. Raunig *et al.*, “Quantitative imaging biomarkers: A review of statistical methods for technical performance assessment,” *Statistical Methods in Medical Research*, vol. 24, no. 1. SAGE Publications Ltd, pp. 27–67, 2015
- [42] C. Messiou, D. J. Collins, S. Giles, J. S. De Bono, D. Bianchini, and N. M. De Souza, “Assessing response in bone metastases in prostate cancer with diffusion weighted MRI,” *Eur Radiol*, vol. 21, no. 10, pp. 2169–2177, 2011.
- [43] I. Lavdas *et al.*, “Apparent diffusion coefficient of normal abdominal organs and bone marrow from whole-body DWI at 1.5 T: The effect of sex and age,” *American Journal of Roentgenology*, vol. 205, no. 2, pp. 242–250, 2015
- [44] S. Keaveney *et al.*, “Image quality in whole-body MRI using the MY-RADS protocol in a prospective multi-centre multiple myeloma study,” *Insights Imaging*, vol. 14, no. 1, pp. 1–14, 2023
- [45] R. Donners, M. Blackledge, N. Tunariu, C. Messiou, E. M. Merkle, and D.-M. Koh, “Quantitative Whole-Body Diffusion - Weighted MR Imaging,” *Magn Reson Imaging Clin N Am*, vol. 26, no. 4, pp. 479–495, 2018
- [46] M. Rata *et al.*, “Implementation of Whole-Body MRI (MY-RADS) within the OPTIMUM/MUKnine multi-centre clinical trial for patients with myeloma,” *Insights Imaging*, vol. 13, no. 1, pp. 1–16, 2022
- [47] J. Ceranka, F. Lecouvet, J. De Mey, and J. Vandemeulebroucke, “Computer-aided detection of focal bone metastases from whole-body multi-modal MRI,” no. March 2020, p. 27, 2020
- [48] R. Donners *et al.*, “Repeatability of quantitative individual lesion and total disease multiparametric whole-body MRI measurements in prostate cancer bone metastases,” *British Journal of Radiology*, vol. 96, no. 1151, 2023
- [49] N. Tunariu *et al.*, “METRADS-P vs. RECIST/PCWG criteria to detect disease progression in metastatic castration-resistant prostate cancer (mCRPC),” *Journal of Clinical Oncology*, vol. 42, no. 16, 2024
- [50] A. Barnes *et al.*, “Guidelines & recommendations: UK quantitative WB-DWI technical workgroup: Consensus meeting recommendations on optimisation, quality control, processing and analysis of quantitative whole-body diffusion-weighted imaging for cancer,” *British Journal of Radiology*, vol. 91, no. 1081, pp. 1–12, 2018
- [51] N. Tunariu *et al.*, “What’s New for Clinical Whole-body MRI (WB-MRI) in the 21st Century,” *Br J Radiol*, vol. 93, pp. 1–13, 2020